Check for
updates

Simulations of Wall Bounded Turbulent Flows Using General Pressure Equation

Xiaolei Shi[1] · Chao-An Lin[1]

Abstract

The general pressure equation (GPE) based method is fully explicit, and the method does not require either solving the pressure Poisson equation nor executing sub-iteration for incompressible flow simulation. However, few numerical validations of GPE method are available, especially under complex flows like turbulence. In this work, GPE is used to conduct direct numerical simulations of the turbulent lid-driven cavity (LDC) flow at Re = 3200 and fully developed turbulent flow through a square duct at $Re_\tau = 360$. Predicted turbulence statistics are compared with existing numerical and experimental data, providing an excellent quantitative agreement. The intricate flow patterns such as the Taylor–Görtler-like vortices in LDC flow and the mean secondary flow at the cross-section in the square duct are captured, showing both qualitative and quantitative agreements with measurements. Results from the present study indicate the capability of the GPE method for accurate incompressible turbulent flow calculation.

Keywords General pressure equation · Direct numerical simulation · Wall bounded flow · Turbulent square duct flow · Turbulent lid-driven cavity flow · Graphics processing unit

1 Introduction

The simulations of incompressible flows (INS) encounter the decoupling between pressure and velocity. To advance the pressure field, numerical schemes which involve solving an additional equation such as the Poisson equation for the pressure correction (Kim and Moin 1985) might be used. Solving the elliptic linear algebra system introduced by pressure Poisson equation is usually the most severe obstacle for both reducing the computational cost or taking advantage of highly parallelism hardware like graphics processing unit (GPU) due to the limitation of parallel efficiency or memory bounded operations.

✉ Chao-An Lin
calin@pme.nthu.edu.tw

Xiaolei Shi
xiaoleishi.th@gmail.com

[1] Department of Power Mechanical Engineering, National Tsing Hua University, Hsinchu 30013, Taiwan

Instead of solving the pressure Poisson equation, a fully explicit approach with locality stencils for the simulation of incompressible flow is desired. Chorin (1967) proposed the artificial compressibility method (ACM), in which artificial compressibility was introduced into the continuity equation as shown in Eq. 1a,

$$\frac{\partial P}{\partial t} + \frac{1}{\delta} \nabla \cdot \mathbf{u} = 0 \tag{1a}$$

$$\frac{\partial P}{\partial t} + \frac{1}{\mathrm{Ma}^2} \nabla \cdot \mathbf{u} = 0 \tag{1b}$$

$$\frac{\partial G}{\partial t} + \frac{1}{\mathrm{Ma}^2} \nabla \cdot \mathbf{u} = \frac{\gamma}{\mathrm{RePr}} \nabla^2 G \quad G = P - E_k \tag{1c}$$

$$\frac{\partial P}{\partial t} + \mathbf{u} \cdot \nabla P + \frac{1}{\mathrm{Ma}^2} \nabla \cdot \mathbf{u} = \frac{1}{\mathrm{Re}} \nabla^2 P \tag{1d}$$

$$\frac{\partial P}{\partial t} + \frac{1}{\mathrm{Ma}^2} \nabla \cdot \mathbf{u} = \frac{\gamma}{\mathrm{RePr}} \nabla^2 P \tag{1e}$$

where δ is the inverse of the square of the artificial speed of sound C_s, i.e. $C_s^2 = 1/\delta$. The AC method was used to obtain steady incompressible flows, so the intermediate results before the final steady-state solutions using large time-step does not satisfy the divergence-free condition. Soh and Goodrich (1988) proposed an unsteady version of AC method. However, sub-iteration is required to ensure the divergence-free at each time step.

An alternative approach, the lattice Boltzmann method (LBM) as a new computational fluid dynamics tool, has been widely used during the last three decades. By adopting the second-order Chapman–Enskog expansion, the macroscopic pressure equation (Eq. 1b) can be recovered from the lattice Boltzmann BGK model (He and Luo 1997; He et al. 2002; Ohwada et al. 2011), where Ma is the Mach number. Equation 1b bears a striking similarity to its AC method counterpart. LBM scheme has been applied to compute turbulent channel flow (Koda and Lien 2015; Kuwata and Suga 2016) and duct flow (Dorschner et al. 2016; Lee et al. 2018). However, the disadvantage of LBM is that the mesh adopted is in general uniform, which poses limitations in simulating turbulent flows at high Reynolds numbers and flows with complex geometry. Thus, there are efforts in developing adaptive mesh or curved coordinate (Kuwata and Suga 2016; Eitel-Amor et al. 2013; Ilio et al. 2018) in improving the predicting capability of LBM.

Further, Ansumali et al. (2005), Karlin et al. (2006) and Borok et al. (2007) proposed the kinetically reduced local Navier–Stokes (KRLNS) equations, based on the low Mach number assumption (Ma $\ll$ 1), as an alternative for the simulation of incompressible flow. In KRLNS the grand potential G instead of the thermodynamic pressure p is coupled with the velocity, as shown in Eq. 1c, where E_k is the kinetic energy, γ, Re, Pr are the heat capacity ratio, Reynolds number and Prandtl number respectively. Several test cases, including 3D Taylor–Green vortex (Karlin et al. 2006), 2D lid-driven cavity flow (Borok et al. 2007), and 3D decaying homogeneous isotropic turbulence (Hashimoto et al. 2018) are simulated, and good agreements with classical INS and LBM are achieved. Though Clausen (2013) claimed that the KRLNS exhibits a qualitatively incorrect evolution of the pressure field due to the absence of $\frac{1}{\mathrm{Re}} \nabla u : \nabla u$ term, Karlin et al. (2006) demonstrated that this term gave a negligible contribution overall

in the range of parameters; besides, the accuracy of KRLNS was further proved through the comparison with LBM and pseudo-spectral method (PSM) (Hashimoto et al. 2018).

Following a similar approach of the KRLNS and introducing the thermodynamic constraint to damp pressure oscillations, Clausen (2013) proposed the entropically damped artificial compressibility (EDAC) method, as shown in Eq. 1d. Note that as Ma → 0, Eqs. 1a, 1b, 1d converge to the INS. However, the EDAC method also converges to the pressure-Poisson equation for Stokes flow as Re → 0. The ability to demonstrate proper behavior at both the viscous (Re → 0) and inertial (Re → ∞) limits makes the EDAC method more physically realistic and superior to its AC counterpart in terms of the time-accurate simulation. Delorme et al. (2017) used EDAC to conduct LES study, and Kajzer and Pozorski (2018) used the scheme to compute direct numerical simulation of turbulent channel flows.

Recently, Toutant (2017) derived the general pressure equation (GPE) based on the isothermal limit and low Mach number assumption, as shown in Eq. 1e. The GPE has a very similar form with the grand potential equation (Eq. 1c) of KRLNS, except the pressure P is coupled directly with the velocity, which simplifies the computation. Difference between the GPE and EDAC locates at the pressure advection term $\mathbf{u} \cdot \nabla P$. During the derivation of GPE (Toutant 2017), this term was neglected for low Mach number assumption. Toutant (2018) indicated that GPE satisfies the exact solutions of the unsteady Taylor–Green vortices, whereas ACM, KRLNS, and EDAC do not. However, for the doubly periodic shear layers, the predicted results between GPE, ACM, and EDAC are marginal (Toutant 2018).

Based on the above, GPE by Toutant (2017) does not contain the convection term as compared to EDAC, which reduces the computational complexity of the numerical procedure and may potentially enhance the numerical stability. Despite the successes of many low Reynolds number flow simulations using GPE (Toutant 2018), the capability of the GPE method to compute turbulent flows, which to the author's knowledge has not been explored. Therefore, the GPE based method is used to perform the direct numerical simulation (DNS) of turbulent lid-driven cavity (LDC) flow of Re = 3200 and fully developed turbulent flow through a square duct of $Re_\tau = 360$. The remainder of this paper is organized as follows: the formulation of the governing equations as well as numerical aspects are given in Sect. 2 and the numerical results of turbulent LDC and fully developed duct flow are presented in Sect. 4. The conclusions of present studies are reported in Sect. 5.

2 Mathematical Formulation

The governing equations for the simulation of incompressible flow by general pressure equation (Toutant 2018) and the momentum equation are given by

$$\frac{\partial P}{\partial t} + \frac{1}{\text{Ma}^2} \nabla \cdot \mathbf{u} = \frac{\gamma}{\text{RePr}} \nabla^2 P \tag{2}$$

$$\frac{\partial \mathbf{u}}{\partial t} + \nabla \cdot (\mathbf{uu}) = -\nabla P + \frac{1}{\text{Re}} \nabla^2 \mathbf{u} + F_i \tag{3}$$

where P is the kinematic pressure, $\mathbf{u}$ is the velocity and F_i represents an external forcing term, $\gamma, \text{Re}, \text{Pr}$ are the heat capacity ratio, Reynolds number and Prandtl number respectively. The Mach number is defined as $\text{Ma} = u_c / C_s$, where C_s is the artificial sound speed and u_c is the characteristic velocity in the flow field. γ / Pr is regarded as a numerical parameter. Equations 2 and 3 converge to the INS equations with an error of $O(\text{Ma})$. Lower Mach

number allows smaller velocity divergence, thus one should keep Ma under a typical small value by adjusting sound speed C_s to keep an acceptable approximation error.

The two numerical parameters, Ma and γ/Pr, need to be determined before calculation. According to Toutant (2018), Ma ≤ 0.05 usually offers a good compromise between the accuracy and a stable time step, which is also a typical value widely used in lattice Boltzmann method. In this work a smaller Ma = 0.01 is adopted to further reduce the continuity error. The coefficient γ/Pr is directly related with the acoustic wave attenuation (Toutant 2018). The assumption of Pr = γ is adopted in present work for it recovers physical relation in doubly periodic shear layers problem and also yields accurate results for both of the test cases (Toutant 2017). For detailed parametric studies of the influence of Ma and γ/Pr on the GPE method can be found in Toutant (2017, 2018).

The governing equations (Eqs. 2, 3) are discretized on a non-uniform staggered grid where pressure is stored at the center of control volume and velocities are stored at the interface as shown in Fig. 1 by using finite-volume approach. Spatial derivatives for velocities and pressure are approximated by second-order central difference scheme. For simplicity, the two-dimensional discretizations of Eq. 2 and the x-component of Eq. 3 are illustrated in Eqs. 4–6. The extension to three-dimension is straightforward

$$
\begin{aligned}
\frac{\partial P_{i,j}}{\partial t} \Delta x_i \Delta y_i &= \frac{1}{\text{Ma}^2} \left[\left(u_{i+1,j} - u_{i,j} \right) \Delta y_i + \left(v_{i,j+1} - v_{i,j} \right) \Delta x_i \right] \\
&+ \frac{\gamma}{\text{RePr}} \left[\left(P_{i+\frac{1}{2},j} - P_{i-\frac{1}{2},j} \right) \Delta y_i + \left(P_{i,j+\frac{1}{2}} - P_{i,j-\frac{1}{2}} \right) \Delta x_i \right]
\end{aligned}
\tag{4}
$$

Fig. 1 Staggered grid configuration
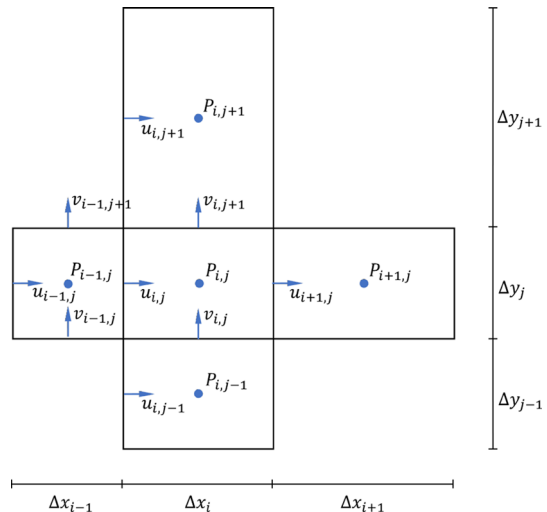
$$\frac{\partial u_{i,j}}{\partial t} \Delta x_i^u \Delta y_j^u = -C_{i,j} - P_{i,j} + \frac{1}{\text{Re}} D_{i,j}$$

$$C_{i,j} = \left([uu]_{i+\frac{1}{2},j} - [uu]_{i-\frac{1}{2},j} \right) \Delta y_j^u + \left([vu]_{i,j+\frac{1}{2}} - [vu]_{i,j-\frac{1}{2}} \right) \Delta x_i^u$$

$$P_{i,j} = \left(P_{i,j} - P_{i-1,j} \right) \Delta y_j^u \tag{5}$$

$$D_{i,j} = \left(\left[\frac{\partial u}{\partial x}\right]_{i+\frac{1}{2},j} - \left[\frac{\partial u}{\partial x}\right]_{i-\frac{1}{2},j} \right) \Delta y_j^u + \left(\left[\frac{\partial u}{\partial y}\right]_{i,j+\frac{1}{2}} - \left[\frac{\partial u}{\partial y}\right]_{i,j-\frac{1}{2}} \right) \Delta x_i^u$$

where $x_i^u = (\Delta x_{i-1} + \Delta x_i)/2$, $\Delta y_j^u = \Delta y_j$, and

$$\begin{cases} P_{i+\frac{1}{2},j} = \frac{\Delta x_{i+1} P_{i,j} + \Delta x_i P_{i+1,j}}{\Delta x_i + \Delta x_{i+1}} \\ P_{i,j+\frac{1}{2}} = \frac{\Delta y_{j+1} P_{i,j} + \Delta y_j P_{i,j+1}}{\Delta y_j + \Delta y_{j+1}} \end{cases} \quad \begin{cases} u_{i+\frac{1}{2},j} = \frac{u_{i,j} + u_{i+1,j}}{2} \\ u_{i,j+\frac{1}{2}} = \frac{\Delta y_{j+1} u_{i,j} + \Delta y_j u_{i,j+1}}{\Delta y_j + \Delta y_{j+1}} \end{cases}$$

$$\begin{cases} v_{i,j+\frac{1}{2}} = \frac{\Delta x_{i,j} v_{i-1,j+1} + \Delta x_{i-1} v_{i,j+1}}{\Delta x_{i-1} + \Delta x_i} \\ v_{i,j-\frac{1}{2}} = \frac{\Delta x_{i,j} v_{i-1,j} + \Delta x_{i-1} v_{i,j}}{\Delta x_{i-1} + \Delta x_i} \end{cases} \quad \begin{cases} \left[\frac{\partial u}{\partial x}\right]_{i+\frac{1}{2},j} = \frac{u_{i+1,j} - u_{i,j}}{\Delta x_i} \\ \left[\frac{\partial u}{\partial x}\right]_{i,j+\frac{1}{2}} = \frac{u_{i,j+1} - u_{i,j}}{(\Delta y_j + \Delta y_{j+1})/2} \end{cases} \tag{6}$$

The temporal integration is performed using the 3rd order TVD Runge-Kutta scheme (Williamson 1980) which reads,

$$Q^{(1)} = Q^n + \Delta t L(Q^n)$$

$$Q^{(2)} = \frac{3}{4} Q^n + \frac{1}{4} \left[Q^{(1)} + \Delta t L(Q^{(1)}) \right] \tag{7}$$

$$Q^{n+1} = \frac{1}{3} Q^n + \frac{2}{3} \left[Q^{(2)} + \Delta t L(Q^{(2)}) \right]$$

where Q represents flow variables u, v, w and p and $L(\cdot)$ is the numerical spatial operator. The stability of such discretized system is restricted by both the diffusive stability requirement and Courant–Friedrichs–Lewy (CFL) condition which are given by:

$$\Delta t_v \cdot \frac{\max(\frac{1}{\text{Re}}, \frac{\gamma}{\text{RePr}})}{\min(\Delta x^2, \Delta y^2, \Delta z^2)} < \frac{1}{2} \tag{8}$$

$$\Delta t_{\text{CFL}} \cdot \frac{u_c/\text{Ma}}{\min(\Delta x, \Delta y, \Delta z)} < 1 \tag{9}$$

A fixed value of CFL = 0.5 is maintained in the present simulations. One should pay attention that in GPE method, characteristic velocity in CFL condition is the numerical sound speed $C_s = u_c/\text{Ma}$ instead of the real velocities in the flow field, which yields a much smaller time step compared with that of INS solver.

In order to capture the fine turbulence structure in the boundary layer, computational grids are clustered to the wall by the following hyperbolic tangent function

$$y_j = \frac{h}{a} \tanh\left(\frac{\xi_j}{2} \ln \frac{1+a}{1-a}\right) \tag{10}$$

with $\xi_j = -1 + \frac{2j}{N}$ where N is the number of grids in the corresponding direction.

3 GPU Implementation

The discretization in Sect. 2 gives a fully explicit system, where only the values of the surrounding points are required for the update of each point. Such explicit treatment and locality make this method naturally parallelizing and especially suitable for the graphics processing unit (GPU).

In the present work, a GPU implementation is built on a hybrid of message passing interface (MPI) and CUDA based on the C++ programming language, in which CPUs are only responsible for the program flow control and file IO. The flow variables are organized by structure of arrays (SoA) format in the GPU memory. We adopt a one-dimensional domain decomposition along the z-direction, as shown in Fig. 2, in which the flow variables allocated in GPU memory are slightly larger to accommodate the "HALO region" for data communication between neighboring GPUs. We rely on the CUDA-Aware MPI (GPU-Direct) for communication on distributed memory system so that explicit data transfer between the host (CPU) and device (GPU) in communication is avoided, which yields more compact code and higher efficiency.
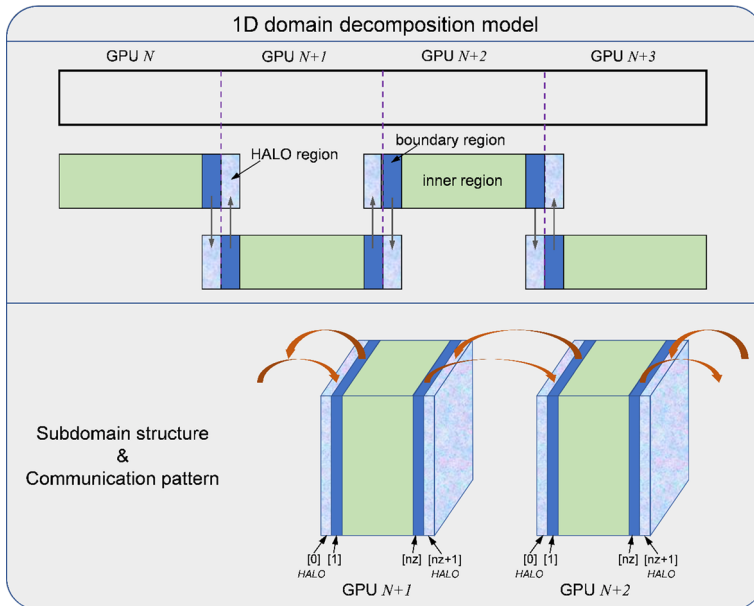
Fig. 2 One-dimensional domain decomposition and communication pattern

We compile the present multi-GPU implementation with Open MPI 3.1.3 and CUDA 10.1 toolkit. The following simulations are performed on multiple NVIDIA GPUs using double precision.

4 Numerical Results

4.1 Turbulent Lid-Driven Cavity Flow

The lid-driven cavity flow is a problem widely investigated due to its relevance to several engineering applications. Flow within the cavity is characterized by the formation of a primary vortex and a few complex secondary vortices. The regular geometry and easily posed boundary condition have made it a popular test case for the validation of numerical schemes.

In the present work, the turbulent flow within a cubic cavity of Reynolds number $Re = u_{lid}L/v = 3200$, based on lid velocity and cavity height ($L = 1$), is explored. The geometry setup and the coordinate system are shown in Fig. 3. The grid density adopted is 192^3, which is symmetry clustered towards the wall using Eq. 10 with $a = 0.8$ in the x, y, and z-directions. For the current grid resolution, we have verified that the cell sizes are of the order of the Kolmogorov length scale (η) given by $\eta = (v^3/\epsilon)^{1/4}$, where ϵ is the dissipation rate of turbulent kinetic energy. At the wall, ϵ has been estimated from the viscous diffusion term in the turbulent kinetic energy equation (Owolabi and Lin 2018). Stationary boundary condition for the velocity is imposed along the cavity walls, except that a constant velocity (u_{lid}) is applied on the cavity lid in the x-direction. Neumann (zero-gradient) boundary condition is applied for the pressure at all walls. The simulation is stopped until a statically steady state is reached after $2000L/u_{lid}$ and is identified by a constant mean shear stress profile.

The distributions of mean velocity and the Reynolds stress along the wall bisector $(x, 0.5, 0.5)$ and $(0.5, 0.5, z)$ at the symmetry plane are presented in Fig. 4. Here the experimental data of Prasad and Koseff (1989) and results of incompressible Navier–Stokes (INS) solver are included for comparison. The results calculated by the GPE method agree well with both the experiments and INS simulations. The unique feature of the 3D lid-driven cavity flow at Reynolds number 3200 compared with its 5000 and 10,000 counterparts is the existence of the Taylor–Görtler-like (TGL) vortices, which accounts for the

Fig. 3 Geometry setup for 3D lid-driven cavity flow. $x: -0.5 \text{ to } 0.5, y: -0.5 \text{ to } 0.5, z: -0.5 \text{ to } 0.5$
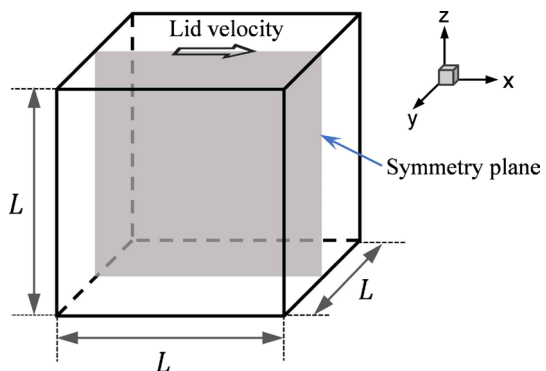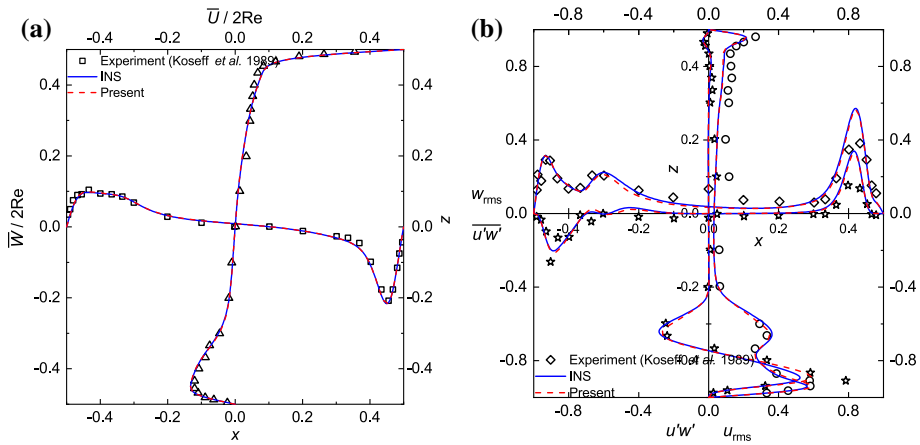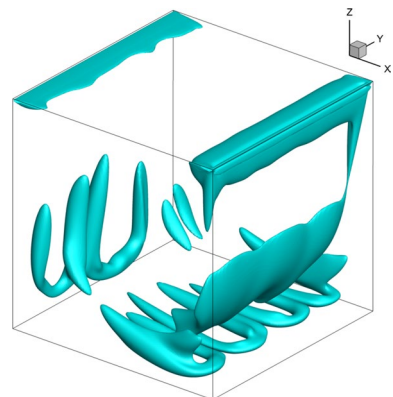
Fig. 4 **a** Mean, **b** Reynolds stress profile along the horizontal and vertical centerlines in the symmetry plane. The symbols are experimental results of Prasad and Koseff (1989)
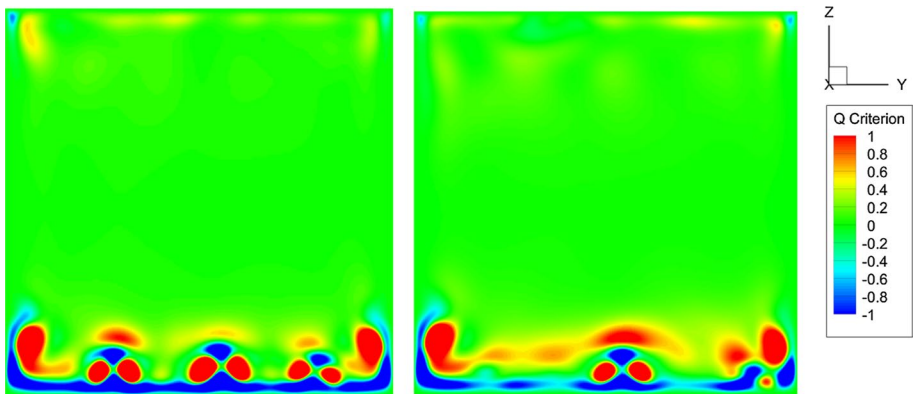
Fig. 5 Vorticity contours at two different times in the $x = 0$ plane, showing the unsteady nature of TGL vortices

Fig. 6 Three-dimensional vorticity structure within cubic cavity of $Q = 1.2$

peak of $\overline{u'w'}$ and u_{rms} in the lower wall vicinity as shown in Fig. 4. Prasad and Koseff (1989) showed that there exists a spanwise (y-direction) meandering of the TGL vortices. This phenomenon is successfully captured by the present method, as demonstrated in Fig. 5. Figure 6 shows the 3D vorticity contours, where the hairpin-like structure at the lower and downstream wall can be observed.

4.2 Turbulent Duct Flow

Turbulent flows along a square duct are of considerable engineering interest due to the relevance to flows in heat exchangers or internal cooling passages of the turbine blade. These flows are characterized by the existence of mean secondary flows of the Prandtl's second kind which appreciably alter the transfer of momentum and scalar quantities near the walls albeit with its relevantly small magnitude (only 1–3% of the streamwise bulk velocity). It is also regarded as a preferable case to test numerical schemes or turbulent models.

In the present work, the Reynolds number has been kept being 360 based on the friction velocity u_τ and the height of the duct H, corresponding to a Reynolds number of 5180 based on bulk velocity u_b. A computational domain with dimensions $2\pi H \times H \times H$ in the x, y and z-direction is used, shown in Fig. 7, which has been verified to be sufficient to ensure the spatial decorrelation of turbulent statistics under such Reynolds number (Madabhushi and Vanka 1991). A corresponding grid number is $384 \times 192 \times 192$ where a nonuniform grid is generated by Eq. 10 with $a = 0.95$ in the y and z directions, yields a grid spacing (Δy^+, Δz^+) varies from 0.6 to 3.9 in the cross-section and $\Delta x^+ = 5.9$ in the streamwise direction. The boundary condition at the duct wall is no slip for velocities and Neumann (zero-gradient) for pressure, and in the streamwise direction, both the velocities and pressure are set to be periodic. Averaging was performed both in time ($30H/u_\tau$ time units to ensure a statistically steady-state) and in the streamwise direction.

The contours of the mean streamwise velocity superimpose on the vector field is shown in Fig. 8a. The bulging of the streamwise velocity contours, induced by the secondary velocities, towards the corners is evident. For comparison, an instantaneous flow field at $x = \pi$ plane is shown Fig. 8b. The mean streamwise velocity distribution normalized with the local friction velocity along the lower wall bisector is given in Fig. 9 and compared with the DNS data of channel flow of $Re_\tau = 180$. The present result is in good agreement with the simulation of Moser et al. (1999).

Distributions of the mean streamwise velocity and V component of the secondary velocity normalized by the maximum mean streamwise velocity are shown in Fig. 10. Good correspondence with results of Gavrilakis (1992) is obtained, indicating the accurate predictions of the secondary flows. The skin friction variation $\tau_w/\overline{\tau}_w$ along the wall is given
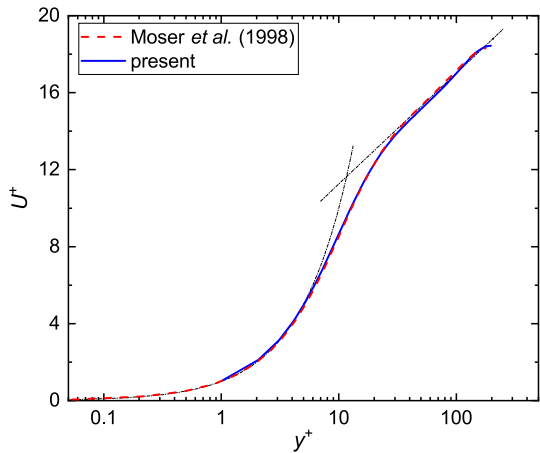

Fig. 7 Geometry setup for square duct flow. $x : 0 \sim 2\pi, y : 0 \sim H, z : 0 \sim H$
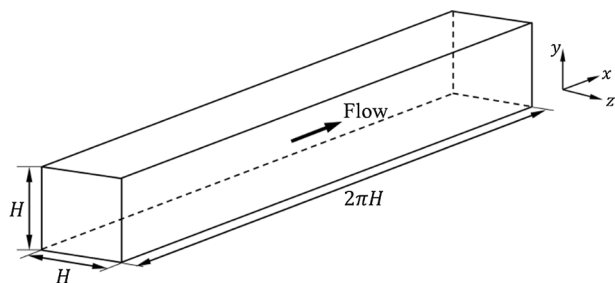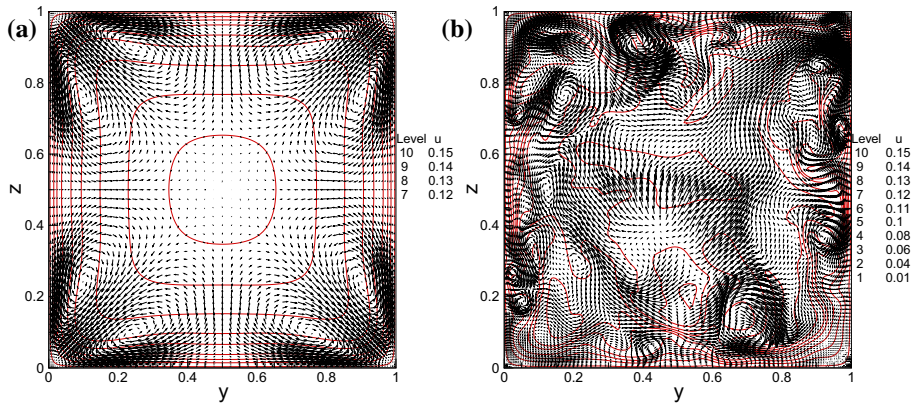
Fig. 8 **a** Contours of mean streamwise velocity and velocity vectors of mean secondary flow. **b** Instantaneous streamwise velocity contours and secondary velocity vector at $x = \pi$

Fig. 9 Mean streamwise velocity along the wall bisector

in Fig. 11 with peak value 1.16 at the wall bisector (1.17 obtained by Gavrilakis). Slight variations among these three sets of data could be attributed to the difference of the simulated Reynolds number, which are respectively at $Re_\tau = 300$ for Gavrilakis (1992) and $Re_\tau = 600$ for Hsu et al. (2012), where the Reynolds number is based on the duct height.

Turbulence intensities and the primary Reynolds stress along the lower wall bisector are presented in Fig. 12, and the channel flow of Moser et al. (1999) ($Re_\tau = 360$ based duct height) and duct data by Gavrilakis (1992) are also included for comparison. Turbulence quantities from the current calculation provide excellent agreement with the data of channel flow. The discrepancies between present results and that of Gavrilakis (1992) may be attributed to the difference in Reynolds number. Also, the root-mean-square of vorticity fluctuations are shown in Fig. 13, showing a good correspondence with the data by Moser et al. (1999). Further, Fig. 14 shows the predicted turbulent kinetic energy budget, and the results are compatible with those from Moser et al. (1999), showing the capability of the present methodology.
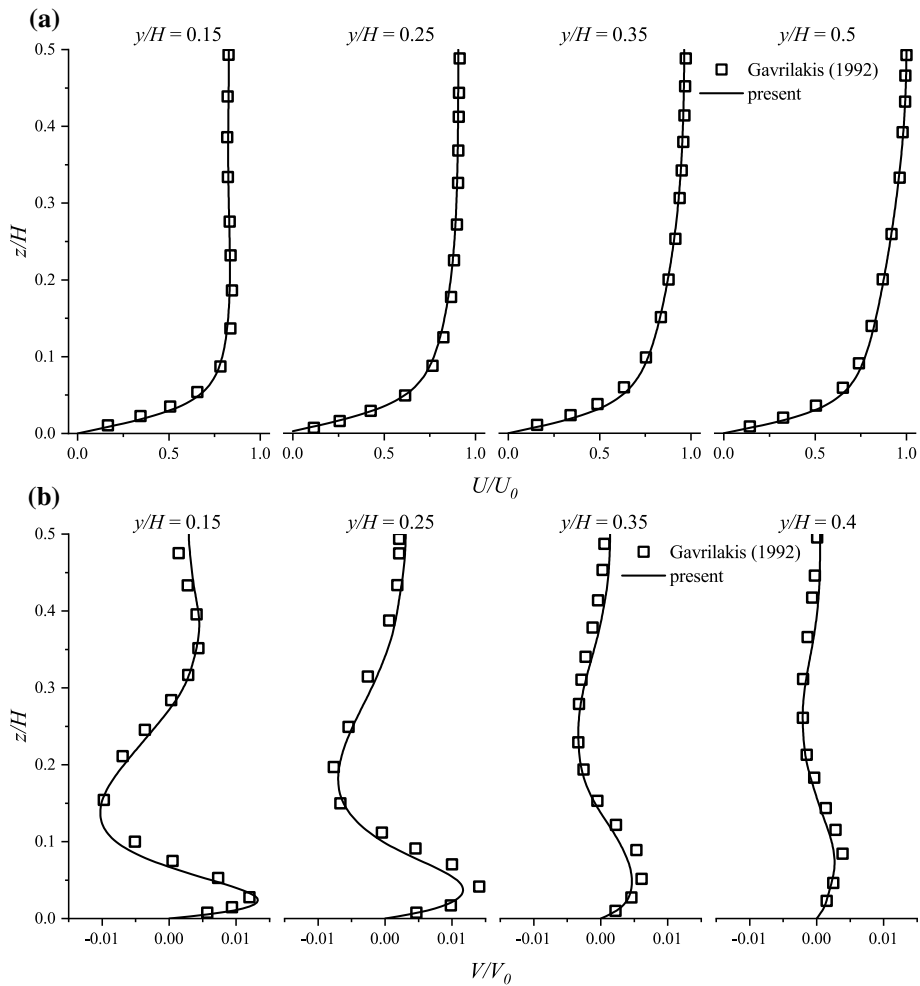
Fig. 10 Comparison of the calculated mean, **a** streamwise, **b** spanwise velocity profile with the simulations of Gavrilakis (1992)

Turbulence anisotropy is further examined by means of the anisotropy invariant map (AIM), where the invariants of the Reynolds stress tensor are defined as $II = -(1/2)b_{ij}b_{ji}$, $III = (1/3)b_{ik}b_{kj}b_{ji}$ where $b_{ij} = \frac{\langle u_i' u_j' \rangle}{\langle u_m' u_m' \rangle} - (1/3)\delta_{ij}$. A realizable pair of $-II$ and III must lie within the Lumley triangle, where the three boundaries are constrained by a two-component state $III = -(II/3 + 1/9)$ and two axisymmetric states $III = \pm 2(-II/3)^{3/2}$. The AIMs of current duct flow at several locations in cross-section are illustrated in Fig. 15. Here the DNS data of channel flow is also included for comparison. The turbulent structure is the same with that of the channel flow at the wall bisector, where turbulence starts at a two-component state from the stationary wall, moves toward the one-component state until $y^+ \approx 16$ ($y^+ \approx 8$ for channel flow) and then follows the rod-like turbulence path towards an isotropic state at the duct center. At the location of $y/H = 0.3$, the AIM shows a similar pattern to that at wall bisector. At a region alongside the sidewall at $y/H = 0.15$, it is expected that the turbulence
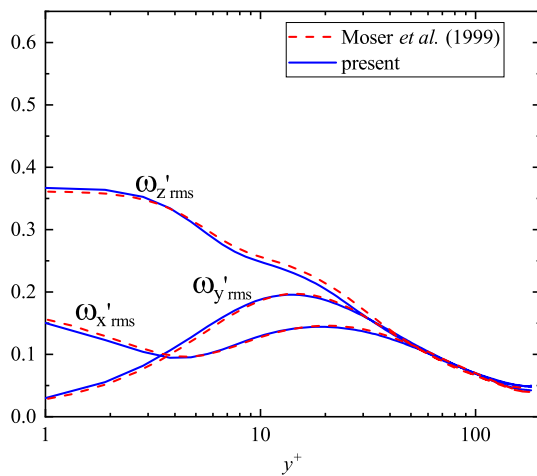
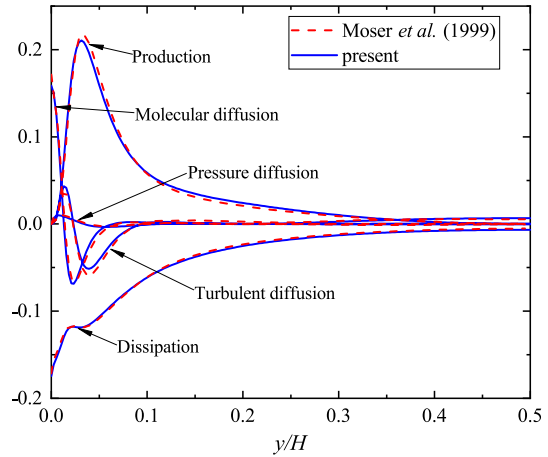**Fig. 11** Variation of wall shear stress along the duct wall
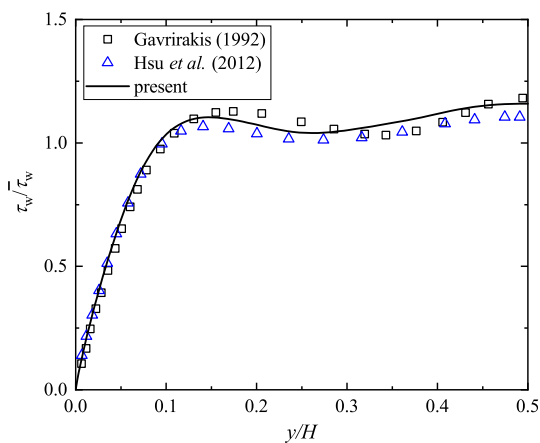
Fig. 12 Distribution of rms fluctuations and the primary Reynolds stress along the wall bisector
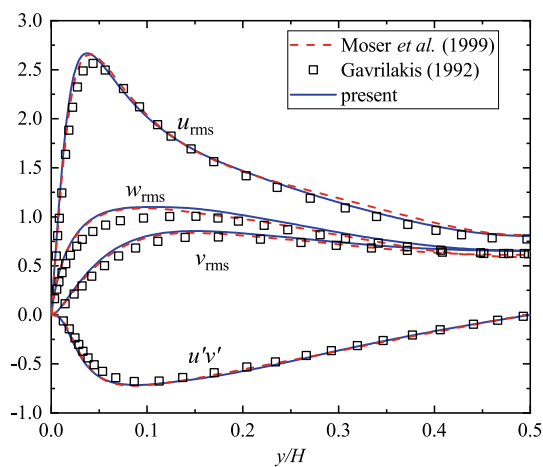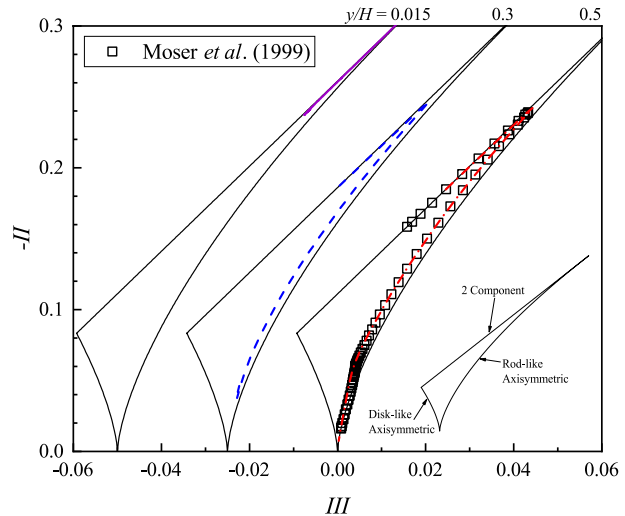

Fig. 13 Rms of vorticity fluctuations along the wall bisector

Fig. 14 Budget of turbulent kinetic energy along the wall bisector

Fig. 15 Anisotropy invariant map at different locations

exhibits a two-component state and turns to one component state at the corner region owning to the strong damping of turbulence both in the y and z directions.

4.3 GPU Performance Comparison of GPE, LBM and DTACM

Here, we compare the GPU performance of GPE relative to the Lattice Boltzmann method (Lee et al. 2018) and the dual time stepping artificial compressibility method (DTACM) (Soh and Goodrich 1988; Shi et al. submitted), where the latter is used for unsteady simulation with sub-iteration to ensure divergence free at each time step. We choose to run the lid-driven cavity flow at Re = 3200 till physical time $t = 1$ for several grid resolutions on

Table 1 Computational time on two NVIDIA V100 GPUs for GPE, LBM, and DTACM

Grid number	Computational time (s)			Wall time ratio	
	GPE	LBM	DTACM	GPE/LBM	DTACM/GPE
192^3	28.27	14.81	182.64	1.91	6.46
256^3	85.65	35.47	414.69	2.41	4.84
384^3	422.63	170.82	1191.29	2.47	2.82
512^3	1375.40	510.35	3272.27	2.70	2.38
768^3	6613.13	NA	NA	NA	NA

The "NA" result is due to out of memory size

two NVIDIA Tesla V100 GPUs, and a uniform grid is used for all test cases. The geometry setup, initial, and boundary conditions are the same as that of Sect. 4.1. The multi-GPU LBM code (D3Q19) used in this comparison is developed by Lee et al. (2018) and has been validated against turbulent duct flow data. The computational time of GPE method is obtained under fixed Ma = 0.05 and CFL = 0.7, and the same Mach number is adopted by LBM. For the DTACM, the stopping criterion of each pseudo time iteration is the satisfaction of continuity, $\sum |\nabla \cdot \mathbf{u}| \leq 10^{-5}$. For LBM simulations, Hong et al. (2015) demonstrated that the GPU outperforms CPU with more than 200 times speedup, showing the superiority of GPU over CPU of explicit scheme. The GPU performance using GPE, LBM and DTACM are summarized in Table 1.

As shown in Table 1, the DTACM is about 5–6.5 times slower than GPE for a small to moderate grid number, due to the excessive sub-iteration required to meet divergence-free criterion. Also, under the present operating conditions, the performance of LBM is about 2.5 times faster than GPE. However, the advantage of GPE over LBM is that the implementation of the non-uniform mesh is straightforward, which is important in simulating the wall-bounded turbulent flows. For that, LBM would require an excessive amount of mesh for high Reynolds number flow due to the uniform grid limitation, or local grid refinement technology (Kuwata and Suga 2016; Eitel-Amor et al. 2013) or curved coordinate (Ilio et al. 2018). Besides, the computational efforts would further increase if the D3Q27 or more elaborate model is employed in LBM, which causes the performance advantage of LBM to decline. At last, the memory size requirement of LBM is much higher than that of GPE based method (19×2 arrays vs. 4×3 arrays).

5 Conclusion

In the present study, the velocity and pressure coupling is achieved by adopting the general pressure equation proposed by Toutant (2017). The method is fully explicit, and the method does not require either solving the pressure Poisson equation nor executing sub-iteration for incompressible flow simulation. Here, the general pressure equation-based method is used to perform the direct numerical simulation of turbulent lid-driven cavity flow at Re = 3200 and fully developed turbulent flow through a square duct at $Re_\tau = 360$. Predicted turbulence statistics are contrasted with existing numerical and experimental

data, providing an excellent quantitative agreement. The intricate flow patterns such as the Taylor–Görtler-like vortices in LDC flow and the mean secondary flow at the cross-section in the square duct are captured, showing both qualitative and quantitative agreements with measurements. Results from the present study indicate the capability of the GPE method for accurate incompressible turbulent flow calculation.

Compliance with Ethical Standards

Conflict of interest The authors declare that they have no conflict of interest

References

Ansumali, S., Karlin, I.V., Öttinger, H.C.: Thermodynamic theory of incompressible hydrodynamics. Phys. Rev. Lett. **94**, 080602 (2005)

Borok, S., Ansumali, S., Karlin, I.V.: Kinetically reduced local Navier–Stokes equations for simulation of incompressible viscous flows. Phys. Rev. E **76**, 066704 (2007)

Chorin, A.J.: The numerical solution of the Navier–Stokes equations for an incompressible fluid. Bull. Am. Math. Soc. **73**(6), 928 (1967)

Clausen, J.R.: Entropically damped form of artificial compressibility for explicit simulation of incompressible flow. Phys. Rev. E **87**, 013309 (2013)

Delorme, Y.T., Puri, K., Nordstrom, J., Linders, V., Dong, S., Frankel, S.H.: A simple and efficient incompressible Navier–Stokes solver for unsteady complex geometry flows on truncated domains. Comput. Fluids **150**, 84 (2017)

Dorschner, B., Bosch, F., Chikatamarla, S.S., Boulouchos, K., Karlin, I.V.: Kinetically reduced local Navier–Stokes equations for simulation of incompressible viscous flows. J. Fluid Mech. **801**, 623 (2016)

Eitel-Amor, G., Meinke, M., Schroder, W.: A lattice-Boltzmann method with hierarchically refined meshes. Comput. Fluids **75**, 127 (2013)

Gavrilakis, S.: Numerical simulation of low-Reynolds-number turbulent flow through a straight square duct. J. Fluid Mech. **244**, 101 (1992)

Hashimoto, T., Yasuda, T., Tanno, I., Tanaka, Y., Morinishi, K., Satofuka, N.: Multi-GPU parallel computation of unsteady incompressible flows using kinetically reduced local Navier–Stokes equations. Comput. Fluids **167**, 215 (2018)

He, X., Luo, L.S.: Lattice Boltzmann model for the incompressible Navier–Stokes equation. J. Stat. Phys. **88**(3), 927 (1997)

He, X., Doolen, G.D., Clark, T.: Comparison of the lattice Boltzmann method and the artificial compressibility method for Navier–Stokes equations. J. Comput. Phys. **179**(2), 439 (2002)

Hong, P.Y., Huang, L.M., Lin, L.S., Lin, C.A.: Scalable multi-relaxation-time lattice Boltzmann simulations on multi-GPU cluster. Comput. Fluids **110**, 1 (2015)

Hsu, H.W., Hsu, J.B., Lo, W., Lin, C.A.: Large eddy simulations of turbulent Couette–Poiseuille and Couette flows inside a square duct. J. Fluid Mech. **702**, 89 (2012)

Ilio, G.D., Dorschner, B., Bella, G., Succi, S., Karlin, I.V.: Simulation of turbulent flows with the entropic multirelaxation time lattice Boltzmann method on body-fitted meshes. J. Fluid Mech. **849**, 35 (2018)

Kajzer, A., Pozorski, J.: Application of the entropically damped artificial compressibility model to direct numerical simulation of turbulent channel flow. Comput. Math. Appl. **76**(5), 997 (2018)

Karlin, I.V., Tomboulides, A.G., Frouzakis, C.E., Ansumali, S.: Kinetically reduced local Navier–Stokes equations: an alternative approach to hydrodynamics. Phys. Rev. E **74**, 035702 (2006)

Kim, J., Moin, P.: Application of a fractional-step method to incompressible Navier–Stokes equations. J. Comput. Phys. **59**(2), 308 (1985)

Koda, Y., Lien, F.S.: The lattice Boltzmann method implemented on the GPU to simulate the turbulent flow over a square cylinder confined in a channel. Flow Turbul. Combust. **94**(3), 495 (2015)

Kuwata, Y., Suga, K.: Imbalance-correction grid-refinement method for lattice Boltzmann flow simulations. J. Comput. Phys. **311**, 348 (2016)

Lee, Y.H., Huang, L.M., Zou, Y.S., Huang, S.C., Lin, C.A.: Simulations of turbulent duct flow with lattice Boltzmann method on GPU cluster. Comput. Fluids **168**, 14 (2018)

Madabhushi, R.K., Vanka, S.: Large eddy simulation of turbulence-driven secondary flow in a square duct. Phys. Fluids A **3**, 2734 (1991)

Moser, R.D., Kim, J., Mansour, N.N.: Direct numerical simulation of turbulent channel flow up to Re $_\tau$ = 590. Phys. Fluids **11**, 943 (1999)

Ohwada, T., Asinari, P., Yabusaki, D.: Artificial compressibility method and lattice Boltzmann method: similarities and differences. Comput. Math. Appl. **61**(12), 3461 (2011)

Owolabi, B.E., Lin, C.A.: Marginally turbulent Couette flow in a spanwise confined passage of square cross section. Phys. Fluids **30**(7), 075102 (2018)

Prasad, A.K., Koseff, J.R.: Reynolds number and end-wall effects on a lid-driven cavity flow. Phys. Fluids A **1**(2), 208 (1989)

Shi, X., Chiu, T.H., Agrawal, T., Lin, C.A., Hwang, F.N.: A parallel nonlinear multigrid solver for unsteady incompressible flow simulation on multi-GPU cluster. J. Comput. Phys. (submitted)

Soh, W., Goodrich, J.W.: Unsteady solution of incompressible Navier–Stokes equations. J. Comput. Phys. **79**(1), 113 (1988)

Toutant, A.: General and exact pressure evolution equation. Phys. Lett. A **381**(44), 3739 (2017)

Toutant, A.: Numerical simulations of unsteady viscous incompressible flows using general pressure equation. J. Comput. Phys. **374**, 822 (2018)

Williamson, J.: Low-storage Runge–Kutta schemes. J. Comput. Phys. **35**(1), 48 (1980)